Engineering 29 (2023) 198–206

Contents lists available at ScienceDirect

Engineering

journal homepage: www.elsevier.com/locate/eng

Research
Electronic Engineering—Article

Transparent Thermally Tunable Microwave Absorber Prototype Based on Patterned VO_2 Film

Zhengang Lu [a,b,*], Yilei Zhang [a,b], Heyan Wang [a,b], Chao Xia [a,b], Yunfei Liu [a,b], Shuliang Dou [c], Yao Li [c], Jiubin Tan [a,b]

[a] Ultra-Precision Optical and Electronic Instrument Engineering Center, Harbin Institute of Technology, Harbin 150001, China
[b] Key Laboratory of Ultra-Precision Intelligent Instrumentation (Harbin Institute of Technology), Ministry of Industry and Information Technology, Harbin 150001, China
[c] Center for Composite Material and Structure, Harbin Institute of Technology, Harbin 150001, China

ARTICLE INFO

Article history:
Received 21 July 2022
Revised 9 September 2022
Accepted 3 October 2022
Available online 12 November 2022

Keywords:
Tunable microwave absorber
VO_2 film
Optical transparent
Near unity absorption
Large modulation depth

ABSTRACT

Transparent microwave absorbers that exhibit high optical transmittance and microwave absorption capability are ideal, although having a fixed absorption performance limits their applicability. Here, a simple, transparent, and thermally tunable microwave absorber is proposed, based on a patterned vanadium dioxide (VO_2) film. Numerical calculations and experiments demonstrate that the proposed VO_2 absorber has a high optical transmittance of 84.9% at 620 nm; its reflection loss at 15.06 GHz can be thermally tuned from –4.257 to –60.179 dB, and near-unity absorption is achieved at 523.750 K. Adjusting only the patterned VO_2 film duty cycle can change the temperature of near-unity absorption. Our VO_2 absorber has a simple composition, a high optical transmittance, a thermally tunable microwave absorption performance, a large modulation depth, and an adjustable temperature tuning range, making it promising for application in tunable sensors, thermal emitters, modulators, thermal imaging, bolometers, and photovoltaic devices.

1. Introduction

The recent, rapid development of optoelectronic devices, including communication and medical devices, and detectors, has made human life more convenient [1–11]. However, optoelectronic devices emit large amounts of electromagnetic radiation [12–14], leading to electromagnetic interference (EMI). Microwave absorbers that can attenuate and even eliminate the adverse effects of microwave radiation are critical for achieving EMI shielding. It is important for microwave absorbers to exhibit efficient microwave absorption and optical transmittance in many applications involving transparent structures, such as windows for communication, medical, and aerospace equipment [15–18].

Recently, efforts have been made to fabricate optically transparent microwave absorbers [19–22]. Wang et al. [19] proposed a transparent perfect microwave absorber employing an asymmetric resonance cavity using graphene and transparent ultrathin doped silver, achieving 99.50% absorption at 13.75 GHz and 93.50% relative visible transmittance. Lai et al. [20] developed an optical transparent flexible broadband absorber based on the indium tin oxide (ITO)–polyethylene terephthalate–ITO structure that achieves a wide absorption bandwidth from 19.9 to 51.8 GHz (absorption > 0.8). However, the transparent microwave absorbers examined rely on geometrical parameters, and thus, once they are designed and fabricated, they exhibit fixed performance characteristics with a constant operating frequency or absorptivity.

Various microwave absorbers with tunable frequency and absorptivity have been recently proposed, with research following two main approaches. In the first approach, various lumped tuning elements, such as varactors and positive–intrinsic–negative (PIN) diodes, are adopted in the structure [23–29]; in this case, tunable microwave absorber performance is achieved by changing the bias voltages applied to the lumped elements. However, this type of absorber requires a complex feed network that is difficult to fabricate and a biasing circuit; generally, such a structure is nontransparent because of the opaque lumped elements. The second approach uses active-controlled materials, such as graphene [29–37], ferroelectric materials [38,39], liquid crystals [40,41], and phase-change materials [42–57]. Among these, VO_2 is a promising candidate for tunable absorbers owing to its drastic

* Corresponding author.
E-mail address: luzhengang@hit.edu.cn (Z. Lu).

https://doi.org/10.1016/j.eng.2022.10.005

insulator-to-metal phase transition (at ~340 K) that leads to transitioning of the sheet resistance magnitude (theoretically five orders of magnitude) and various transition-triggering mechanisms (such as thermal heating, optical excitation, and bias voltage). However, most studies on VO_2 tunable absorbers have focused on the terahertz [42–48] and infrared bands [49–57]; particularly, the experimental verification of VO_2 tunable absorbers requires further reporting. In the few reported experiments on VO_2 tunable terahertz absorbers, the absorbers utilize complete VO_2 films, resulting in an opaque tunable terahertz absorber since the VO_2 film optical transmission is almost zero in the visible band. To the best of our knowledge, the use of VO_2 tunable microwave absorbers for visual observation remains unreported.

Here, a transparent thermally tunable microwave absorber is proposed for the first time based on a patterned VO_2 film that has a simple structure comprising a top-patterned VO_2 film, transparent substrate (quartz glass), and bottom transparent reflective layer (double-layer ITO (D-ITO)). Thermally controlling the VO_2 film sheet resistance enabled the microwave reflection loss (RL) amplitude to be tuned from −4.257 to −60.179 dB. Particularly, a near-unity (99.993%) absorption peak at 15.060 GHz was achieved at 523.750 K, while the optical transmittance was 84.900% at 620.000 nm. Furthermore, the temperature required to achieve near-unity absorption can be tuned by varying the patterned VO_2 film duty cycle. The superior characteristics of the proposed VO_2 absorber suggest that it can be promising for transparent tunable microwave absorbers.

2. Methods

2.1. Fabricating VO_2 films

We deposited the VO_2 films on quartz glass (silicon dioxide, 15.6 mm × 7.7 mm) using a high-power impulse magnetron sputtering system (MS650C; Shengyang KEYOU Vacuum Technology Co., Ltd., China) with a pure vanadium target (99.99%, 3.00 in (1 in = 2.54 cm); Beijing Gold Crown for the New Material Technology Co., Ltd., China). The sputtering deposition temperature and duration were 823.15 K and 55.00 min, respectively. We fixed the power, pulse width, and frequency at 200 W, 50 μs, and 200 Hz, respectively. The working pressure was set to 0.9 Pa using pure argon (Ar) and oxygen (O_2) at a ratio of 80.0/0.4.

2.2. Fabricating VO_2 absorber sample

The fabrication process for the VO_2 absorber sample can be divided into two stages: fabricating the transparent reflective layer at the bottom and the patterned VO_2 films on the top. The transparent reflective layer that acts as a heater is composed of ITO (8 Ω per square ($\Omega \cdot sq^{-1}$), 40 mm × 40 mm; Luoyang Shangzhuo Technology Co., Ltd., China) and aluminum foil (20 mm × 20 mm; Shenzhen Jingzhe Technology Co., Ltd., China). The aluminum foil was cut into a long strip of 0.8 mm × 10.0 mm and pasted onto the ITO film surface using conductive silver paint (Ag and Cu; Jinyi Technology Co., Inc., China), as shown in Fig. S1 in Appendix A. The aluminum foil and ITO were fixed for 15 h at 30 °C to ensure a reliable electrical connection between them.

Patterned VO_2 samples with different duty cycles were fabricated using the same process. First, we pretreated the VO_2 film surface, and a photoresist layer (1 μm thick, AR4400-05 photoresist) was patterned using vacuum contact lithography (URE-2000/35 L; Institute of Optics and Electronics, Chinese Academy of Sciences, China) and the corresponding chromium masks. Then, the VO_2 film without photoresist protection was etched using a reactive ion etching machine (ME-3A; Institute of Microelectronics, Chinese Academy of Sciences, China). The working pressure, power, and duration of etching were 5 mTorr (1 mTorr = 0.133 Pa), 100 W, and 1 min, respectively. Pure sulfur hexafluoride (SF_6) and O_2 were used as the etching gases at flow rates of 54 and 6 standard cubic centimeters per minute (sccm), respectively. Patterned VO_2 samples were obtained after removing the photoresist.

2.3. Sample characterization

The optical transmittance of the VO_2 absorber sample was measured using an ultraviolet (UV)–visible (VIS)–near-infrared (NIR) spectrophotometer (Lambda 950 UV/VIS/NIR Spectrometer, PerkinElmer, USA). The VO_2 absorber was microwave characterized (RL and shielding effectiveness (SE)) in the Ku band utilizing a vector network analyzer (E5071C; Keysight, USA; 300 kHz–20 GHz) with a Ku band-slotted waveguide (HD-140WCAN, Henda Microwave, China). We used a double-testing digital four probe tester (ST2263, Suzhou Jingge Electronic Co., Ltd., China) to measure the square resistance of the VO_2 film at various temperatures. The VO_2 content in the film was determined by X-ray photoelectron spectroscopy (XPS; EscaLab 250Xi; Thermo Fisher Scientific, USA). The XPS data were calibrated to the C1s peak and analyzed using the XPSPEAK software. The fabricated VO_2 absorber sample was micrographed using a three-dimensional (3D) measuring laser microscope OLS5000 (Olympus Corporation, Japan). The Raman spectra of the VO_2 films and patterned VO_2 film were measured using a micro-Raman spectrometer (Renishaw inVia Reflex; Renishaw, UK) with 532 nm laser wavelength.

3. Absorber design and theoretical analysis

3.1. Absorber design

A schematic diagram of the proposed transparent thermally tunable microwave absorber based on a patterned VO_2 film is shown in Fig. 1. The absorber consists of three layers: The top, middle, and bottom layers are a patterned VO_2 film, transparent substrate, and transparent reflective layer, respectively. In this study, thermal heating is the transition-triggering mechanism for the insulator-to-metal phase transition of the VO_2 film, and the independent small rings in Fig. 1 represent the patterned VO_2 film that shows color changes from dark gray (Fig. 1(b)) to dark green (Figs. 1(c) and (d)) with increasing temperature (Fig. S2 in Appendix A). The patterned VO_2 film comprises an array of unit cells. The unit cell of the proposed tunable absorber is shown by the red frame in Fig. 1(a). The absorber parameters are as follows: period $P = 2.000$ mm, ring radius $R_{VO_2} = 0.995$ mm, VO_2 film thickness $h_{VO_2} = 200.000$ nm, quartz glass thickness between the VO_2 film and ITO $h_1 = 2.500$ mm, thickness of the ITO film $h_{ITO} = 200.000$ nm, and quartz glass thickness between the two layers of the D-ITO $h_2 = 1.400$ mm. The VO_2 film used here is a monoclinic phase VO_2 film that displays phase transition behavior (the Raman spectra of the VO_2 film at different temperatures and the Raman spectra of the patterned VO_2 film are shown in Figs. S3 and S4 in Appendix A). The measured sheet resistance of the VO_2 film shows a transition of three orders of magnitude caused by heating and cooling, resulting in a value less than that achieved by the theoretical resistance transition of five orders of magnitude, as shown in Fig. 2(a). This is because the VO_2 content of the film used is only 73.2% (the content was calculated based on the ratio of the areas under the VO_2 peaks to the total area under all of the peaks, as shown in Fig. S5 in Appendix A). The D-ITO, which has a high normalized optical transmittance of 94.29% at 620.00 nm (Fig. S6 in Appendix A) and an electromagnetic SE of more than 40 dB (Fig. S7 in Appendix A) in the Ku band (12–18 GHz), was selected as the transparent reflective layer. Quartz glass was the transparent substrate adopted to separate the

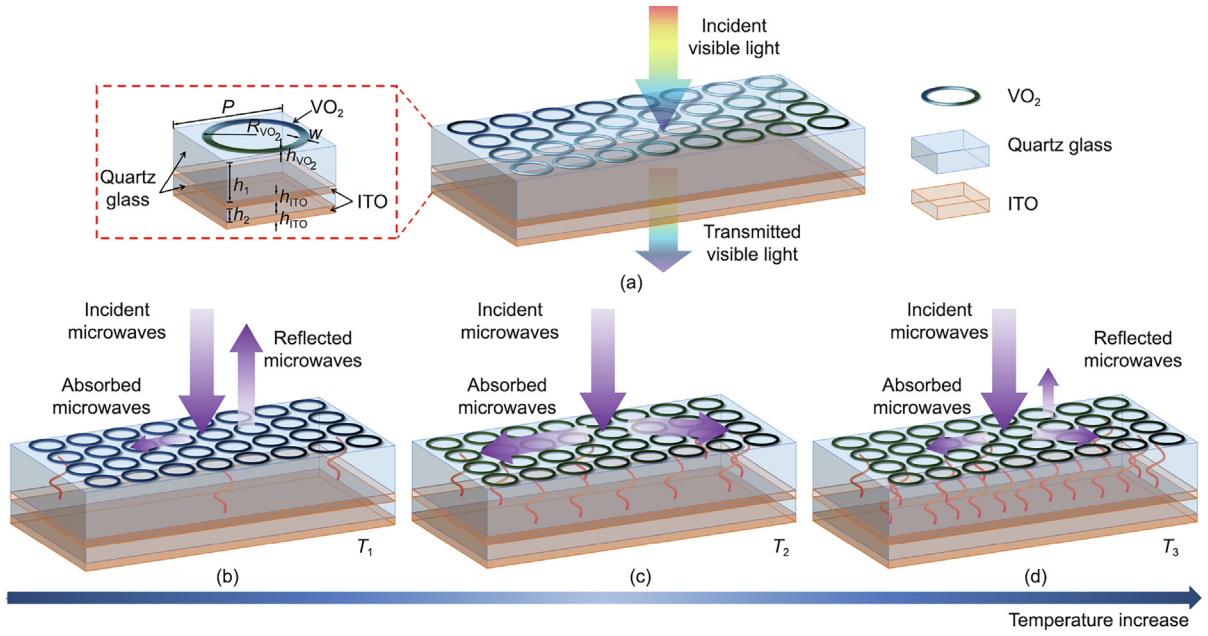

Fig. 1. Transparent thermally tunable microwave absorber based on a patterned VO_2 film. (a) Schematic diagram of the absorber. The red frame shows the unit cell of the absorber. (b–d) Schematic diagram of the absorber under three typical temperatures (T_1, T_2, and T_3), $T_1 < T_2 < T_3$; as the temperature increases, the absorber exhibits different microwave absorption performances with different absorption amplitudes. (b) At T_1, which is close to 302.15 K, most of the incident microwave is reflected. (c) At a given temperature T_2, the incident microwave is almost completely absorbed. (d) At $T_3 > T_2$, most of the incident microwave is absorbed, and the rest is reflected. *P*: period; h_1: quartz glass thickness between the VO_2 film and ITO; h_2: quartz glass thickness between the two layers of the D-ITO; h_{ITO}: thickness of the ITO film; R_{VO_2}: ring radius; h_{VO_2}: VO_2 film thickness; *w*: ring linewidth.

patterned VO_2 film from the transparent reflective layer. Moreover, D-ITO acted as a heater, as shown in Fig. S1, and aluminum foil was used as the electrode to supply voltage to D-ITO to achieve different temperatures.

3.2. Theoretical analysis

The transfer matrix method is a powerful tool to analyze the absorption performance of microwave absorbers. A transfer matrix method based on the equivalent circuit and transmission line theories was adopted to extract the sheet resistance and frequency-dependent absorption of the VO_2 absorber. As shown in the red frame in Fig. 2(b), the patterned VO_2 film on the top layer was modeled as a series equivalent circuit composed of inductance L_1, capacitance C_1, and resistance R_1 based on the equivalent circuit theory [58]. The values of L_1 and C_1 are influenced by the shape and dimensions of the patterned VO_2 film, whereas the value of R_1 depends on the duty cycle D and sheet resistance R_S of the VO_2 film, and $R_1 = R_S/D$. The equivalent impedance Z_1 of the patterned VO_2 can be expressed as [58]

$$Z_1 = R_1 + j\omega L_1 + \frac{1}{j\omega C_1} \tag{1}$$

where j is an imaginary unit. $\omega = 2\pi f$ is the angular frequency of the incident wave. f is the microwave frequency.

According to the transmission line theory, the transfer matrix $[\boldsymbol{V}]$ of the patterned VO_2 film is given by

$$[\boldsymbol{V}] = \begin{pmatrix} 1 & 0 \\ \frac{1}{Z_1} & 1 \end{pmatrix} = \begin{pmatrix} 1 & 0 \\ \frac{1}{R_1 + j\omega L_1 + \frac{1}{j\omega C_1}} & 1 \end{pmatrix} \tag{2}$$

Both quartz glass and the ITO film can be regarded as transmission lines with certain lengths and characteristic impedances, and their transfer matrix is expressed as [59]

$$\begin{pmatrix} \cosh\gamma h & -Z\sinh\gamma h \\ -\frac{1}{Z}\sinh\gamma h & \cosh\gamma h \end{pmatrix}^{-1} \tag{3}$$

where Z is the normalized characteristic impedance, γ is the propagation constant of the material, and h is the thickness of the material. Z and γ are expressed as

$$\begin{aligned} Z &= \frac{1}{Z_0}\sqrt{\frac{\mu}{\varepsilon}} = \frac{1}{Z_0}\sqrt{\frac{\mu}{\varepsilon' + j\sigma/\omega}} \\ \gamma &= \omega\sqrt{\mu\varepsilon} = \omega\sqrt{\mu(\varepsilon' + j\sigma/\omega)} \\ \sigma &= \frac{1}{\rho} = \frac{1}{R_S h} \end{aligned} \tag{4}$$

where $Z_0 = 377\ \Omega$ is the impedance of free space, ε is the permittivity, ε' is the real part of the permittivity, μ is the permeability of free space, σ is the electric conductivity, and ρ is the resistivity. The electric conductivity σ is inversely related to the resistivity ρ and sheet resistance R_S (see Note. S1 in Appendix A for simplification). Based on Eqs. (1)–(4), the total transfer matrix $[\boldsymbol{M}]$ of the patterned VO_2 absorber is related to the transfer matrices of each section as follows:

$$\begin{aligned} [\boldsymbol{M}] = {} & \begin{pmatrix} 1 & 0 \\ \frac{1}{R_1 + j\omega L_1 + \frac{1}{j\omega C_1}} & 1 \end{pmatrix} \\ & \times \begin{pmatrix} \cosh\gamma_{quartz} h_1 & -Z_{quartz\ glass}\sinh\gamma_{quartz} h_1 \\ -\frac{1}{Z_{quartz\ glass}}\sinh\gamma_{quartz} h_1 & \cosh\gamma_{quartz} h_1 \end{pmatrix}^{-1} \\ & \cdots \times \begin{pmatrix} \cosh\gamma_{ITO} h_{ITO} & -Z_{ITO}\sinh\gamma_{ITO} h_{ITO} \\ -\frac{1}{Z_{ITO}}\sinh\gamma_{ITO} h_{ITO} & \cosh\gamma_{ITO} h_{ITO} \end{pmatrix}^{-1} \\ & \times \begin{pmatrix} \cosh\gamma_{quartz} h_2 & -Z_{quartz\ glass}\sinh\gamma_{quartz} h_2 \\ -\frac{1}{Z_{quartz\ glass}}\sinh\gamma_{quartz} h_2 & \cosh\gamma_{quartz} h_2 \end{pmatrix}^{-1} \\ & \cdots \times \begin{pmatrix} \cosh\gamma_{ITO} h_{ITO} & -Z_{ITO}\sinh\gamma_{ITO} h_{ITO} \\ -\frac{1}{Z_{ITO}}\sinh\gamma_{ITO} h_{ITO} & \cosh\gamma_{ITO} h_{ITO} \end{pmatrix}^{-1} = \begin{pmatrix} m_{11} & m_{12} \\ m_{21} & m_{22} \end{pmatrix} \end{aligned} \tag{5}$$

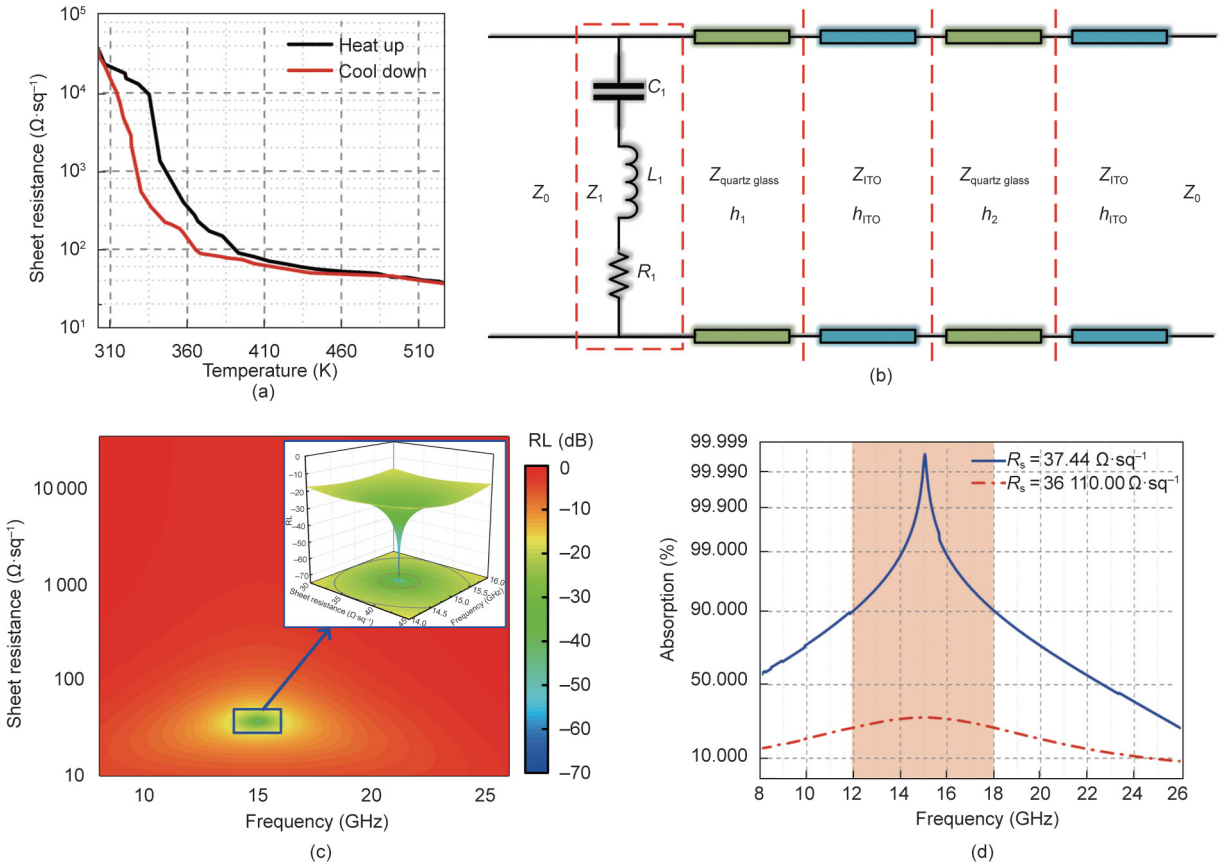

Fig. 2. Measured sheet resistance of the VO_2 film, equivalent circuit model, and calculation results of the VO_2 absorber. (a) Measured sheet resistance of the VO_2 film versus temperature. (b) Equivalent circuit model of the VO_2 absorber. (c) Relationship between the sheet resistance of the VO_2 film and the calculated absorption results of the VO_2 absorber in the 8–26 GHz band. The inset in (c) is the enlarged 3D view of the contour plots at varying sheet resistances in the range of 30–45 $\Omega{\cdot}sq^{-1}$ in the 14–16 GHz band. The contour lines of −20 and −30 dB are plotted by blue and red dashed lines, respectively. (d) Calculated absorption of the VO_2 absorber versus frequency for the sheet resistance values of the VO_2 film of 37.44 and 36 110.00 $\Omega{\cdot}sq^{-1}$. $Z_0 = 377\ \Omega$ is the impedance of free space; L_1 is the inductance; R_1 is the resistance; C_1 is the capacitance; Z_1 is the equivalent impedance of the patterned VO_2; $Z_{quartz\ glass}$ is the normalized characteristic impedance of the quartz glass; Z_{ITO} is the normalized characteristic impedance of the ITO.

where m_{11}, m_{12}, m_{21}, and m_{22} are the value of the elements of $[\boldsymbol{M}]$, γ_{quartz} is the propagation constant of the quartz glass, $Z_{quartz\ glass}$ is the normalized characteristic impedance of the quartz glass, γ_{ITO} is the propagation constant of the ITO, Z_{ITO} is the normalized characteristic impedance of the ITO.

According to the relationship between the transfer matrix and the *S*-parameter matrix, reflection coefficient S_{11} and transmission coefficient S_{21} of the absorber can be expressed as follows:

$$S_{11} = \frac{m_{11} + m_{12} - m_{21} - m_{22}}{m_{11} + m_{12} + m_{21} + m_{22}}$$
$$S_{21} = \frac{2}{m_{11} + m_{12} + m_{21} + m_{22}} \quad (6)$$

The RL, SE, and absorptance (A) are obtained using the reflection coefficient and transmission coefficient as follows:

$$SE = 10 \times \lg(|S_{21}|^2)$$
$$RL = 10 \times \lg(|S_{11}|^2) \quad (7)$$
$$A = 1 - |S_{11}|^2 - |S_{21}|^2$$

Using the above equations, we calculated the RL at 8–26 GHz versus the sheet resistance. The calculation results show that the RL undergoes a shift as the sheet resistance increases, as shown in Figs. 2(c) and (d). At 302.15 K, the VO_2 films have a maximum sheet resistance of 36 110 $\Omega{\cdot}sq^{-1}$ and are insulating, as shown in Fig. 2(a), the calculated reflection capacity of the VO_2 absorber is the highest, whereas its absorption capacity is the lowest. The peak absorption of 28.4% (red dash-dotted line in Fig. 2(d)) is also due to the absorption capacity of D-ITO (the conductivity of ITO is 7.14×10^5 $S{\cdot}m^{-1}$), and the peak absorption can be reduced by increasing the conductivity of the ITO film (Fig. S8 in Appendix A). As the sheet resistance of the VO_2 films decreases from 36 110.00 to 37.44 $\Omega{\cdot}sq^{-1}$, the peak RL of the VO_2 absorber decreases from −1.451 to −62.870 dB, indicating that the VO_2 absorber has a large modulation depth for RL. As shown in Fig. 2(d), at 37.44 $\Omega{\cdot}sq^{-1}$, the VO_2 films are resistive, and the absorber achieves near-perfect impedance matching to free space, resulting in the best performance of the VO_2 absorber; it achieves a bandwidth of more than 90% absorptance from 11.88 to 18.11 GHz, and the peak absorption is near-unity at 15.05 GHz. However, due to an impedance mismatch occurring with the decrease in VO_2 film sheet resistance, the peak absorption decreases when the VO_2 film sheet resistance decreases further.

The VO_2 film sheet resistance is temperature dependent and decreases monotonically with increasing temperature, as shown in Fig. 2(a). Therefore, the VO_2 absorber exhibits thermally tunable absorption performance, as shown in Fig. 2(c). Additionally, the calculation results show that the VO_2 absorber has a large modulation depth.

3.3. Impedance matching analysis

The absorption mechanism is the synergistic result of impedance matching and microwave attenuation capability. The physical cause of microwave attenuation is the Joule heat loss caused by

conductivity, which dissipates microwave energy into heat energy. An equivalent transmission line model was developed to analyze the impedance matching under different frequencies with different sheet resistances (Fig. S9 in Appendix A). Due to the strong electromagnetic SE, the transparent reflective layer of D-ITO is modeled as a short circuit. The input impedance Z_{in} of the VO_2 absorber can be expressed as $\frac{1}{Z_{in}} = \frac{1}{Z_1} + \frac{1}{Z_2}$ (where Z_2 is the equivalent impedance consisting of D-ITO short circuit and quartz glass transmission line see Note. S2 in Appendix A for the solution procedure). The reflection coefficient r is related to the input impedance Z_{in} and free space impedance Z_0 and can be expressed as $r = \frac{Z_{in}-Z_0}{Z_{in}+Z_0}$ for the VO_2 absorber. The reflection coefficient r should be equal to zero to achieve high absorption performance, that is, the real and imaginary parts of impedance matching (Z_{in}/Z_0) are close to one and zero, respectively. Fig. 2(c) shows that the absorption is low when the sheet resistance exceeds 200 $\Omega \cdot sq^{-1}$, so that the real and imaginary parts of Z_{in}/Z_0 are only analyzed for the sheet resistance in the 10–200 $\Omega \cdot sq^{-1}$ range as shown in Figs. 3(a) and (b).

Fig. 3 demonstrates that the VO_2 absorber achieves perfect impedance matching at 15.05 GHz with a real part of 1 and an imaginary part of 0 when the sheet resistance is 34.20 $\Omega \cdot sq^{-1}$. The sheet resistance is lower than the value 37.44 $\Omega \cdot sq^{-1}$ obtained by the transfer matrix method; this is because the transmission line method models D-ITO as a short circuit, idealizing the conductivity of D-ITO.

4. Results

4.1. Experimental verification

To experimentally demonstrate the high optical transmittance and thermally tunable absorption performance of the proposed VO_2 absorber, we fabricated a VO_2 absorber sample and measured its optoelectronic properties. The inset of Fig. 4 (a) shows that the fabricated VO_2 absorber sample exhibits good optical transparency, such that the logo below the sample can be seen with the naked eye. Figs. S10–S12 in Appendix A show the photographs and micrographs of the fabricated VO_2 absorber sample. Fig. 4 (a) shows the transmittance spectra of the fabricated VO_2 absorber sample in the range of 300.00–1000.00 nm at 303.15 and 390.00 K (higher than the phase transition temperature). At 303.15 K, the average normalized transmittance is approximately 77% in the visible range (380–780 nm), the normalized transmittance reaches 78.89% at 550.00 nm (the most sensitive wavelength to the human eye), and the peak normalized transmittance reaches 84.9% at 620.0 nm. The fluctuation in the optical transmittance is due to the optical performance of D-ITO (Fig. S6). The transmittance spectrum at 390.00 K is almost coincident with that at 303.15 K, indicating that the temperature negligibly influences the visible transmittance.

The microwave absorption performance of the fabricated VO_2 absorber samples was measured using a vector network analyzer system. Figs. 4(b) and (c) and Fig. S13 in Appendix A show the contour plots of the measured RL and SE versus frequency and temperature, respectively. The SE is less than −40 dB for all measurements in the temperature range of 303.15–524.85 K, indicating almost zero transmission. The absorption is approximately estimated by $A = 1 - R$, where R is the reflectivity and calculated as $R = 10^{\frac{RL}{10}} \times 100\%$ using the measured RL. Near 303.15 K, the VO_2 film exists in insulator phase and the peak RL of the fabricated VO_2 absorber sample is −4.257 dB. Moreover, the RL of the fabricated VO_2 absorber sample agrees with that of the D-ITO absorber (Fig. S14 in Appendix A) composed of quartz glass with the same thickness and D-ITO, demonstrating that, at 303.15 K, the absorption capacity is attributed to D-ITO, and the patterned VO_2 film has little effect. The fabricated VO_2 absorber sample exhibited a variation of approximately –55.922 dB in the peak RL (from –4.257 to –60.179 dB) at 15.06 GHz when the temperature increased from 303.15 to 523.75 K, indicating that the VO_2 absorber exhibits thermally tunable absorption and a large modulation depth. The fabricated VO_2 absorber sample achieved a SE and RL of –41.756 and –60.179 dB, respectively, and an absorption of 99.993% at 15.060 GHz when the temperature was 523.750 K. At this temperature, VO_2 exists in the metallic phase, allowing the absorber to perfectly match the free space to achieve peak absorption. The absorption bandwidth of the fabricated VO_2 absorber sample reaches approximately 5.22 GHz (corresponding to the range of 12.72–17.94 GHz, as shown in Fig. 4(d) for absorption $\geq$ 90%, almost covering the full Ku band). The peak absorption decreased to 99.990% when the temperature was increased above 524.850 K, possibly due to impedance mismatch. The measured results agree with the calculated predictions shown in Fig. 2(d) and validate the thermally tunable absorption performance and large modulation depth of the proposed absorber. Besides, according to the temperature-dependent reproducibility experiments of the fabricated VO_2 absorber sample (Fig. S15 in Appendix A), the proposed absorber is reusable and stable when temperature cycling, making it is extremely valuable for practical applications.

Additionally, the change in RL with temperature variation is due to the change in impedance matching conditions at the interface between free space and the absorber and the change in impedance matching conditions caused by the different sheet resistances of the VO_2 film. A comparison of Figs. 4(b) and (c) shows that the temperature-dependent RL during the heating process is slightly different from that during the cooling process at the same temperature. This is because the sheet resistance exhibits a small hysteresis, as shown in Fig. 2(a), such that the temperature required to

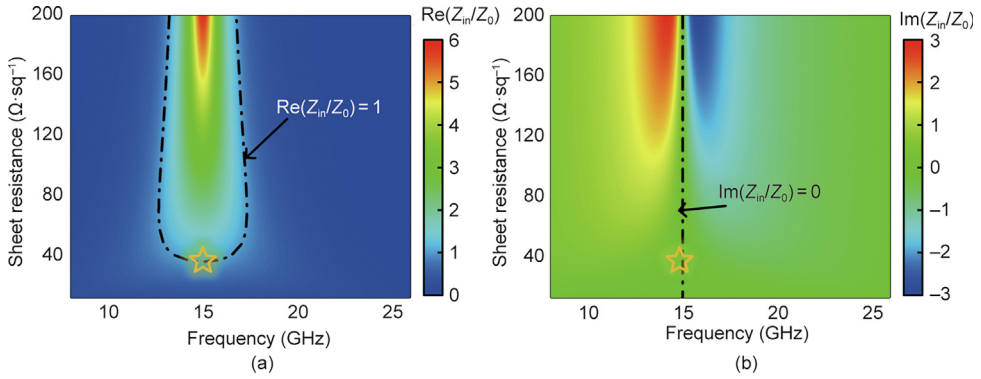

Fig. 3. Relationship between the VO_2 film sheet resistance and the calculated results of impedance matching degree (Z_{in}/Z_0) when the VO_2 film sheet resistance is between 10 and 200 $\Omega \cdot sq^{-1}$. (a) The real parts; (b) the imaginary parts. Re: real part; Im: imaginary part.

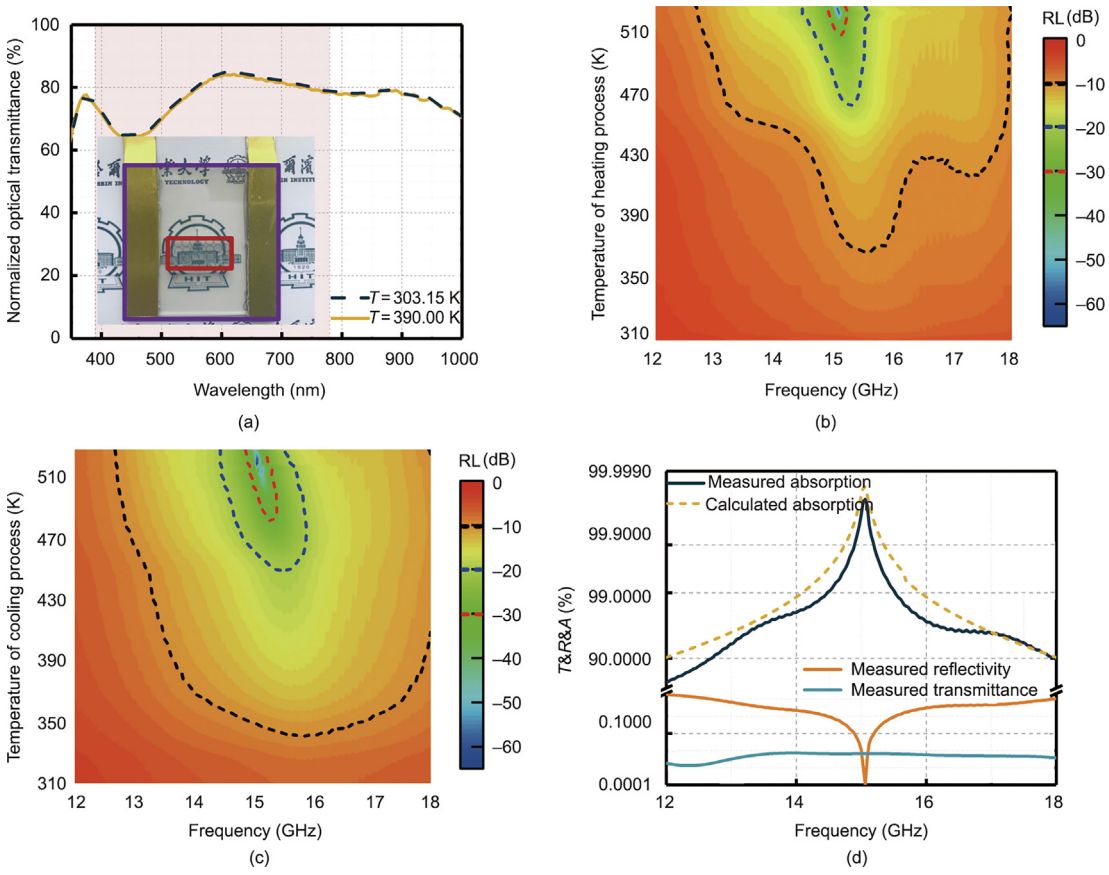

Fig. 4. Measured optical transmittance and microwave absorption of the fabricated VO_2 absorber sample. (a) Normalized optical transmittance; the pink shaded area is the area of the visible band, and the inset is a photograph of the VO_2 absorber. The inset in (a) shows a photograph of the fabricated absorber sample (the original photograph in Fig. S10 in Appendix A). The D-ITO sample is framed in purple, and the VO_2 absorber sample is framed in red. Contour plots of the RL versus frequency and temperature of the fabricated VO_2 absorber sample during the (b) heating process and (c) cooling process. The contour lines of −10, −20, and −30 dB are plotted with black, blue, and red dashed lines, respectively. (d) Comparison of the measured absorption, reflectivity, and transmittance at 523.75 K and calculated absorption at a sheet resistance of 37.44 $\Omega \cdot sq^{-1}$. T&R&A: transmittance & reflectivity & absorption.

achieve a certain sheet resistance in the heating process is higher than that in the cooling process. Therefore, the RL changes slower during the cooling process.

4.2. Adjustable temperature tuning range

The VO_2 absorber sample fabricated in this study achieved a high optical transmittance, thermally tuned absorption performance, and large modulation depth. However, the temperature tuning range and the temperature to achieve near-unity absorption of this absorber were fixed at 303.15–524.85 and 524.85 K, respectively. The temperature tuning range is determined by the temperature that achieves near-unity absorption. To adapt to different thermal environments and broaden the application of our tunable VO_2 absorber, we investigated a method to achieve an adjustable temperature for near-unity absorption. According to the mechanism of near-unity absorption, achieving a perfect match with free space at different temperatures is vital.

According to Eq. (5), near-unity absorption should be constant if R_1 is maintained. R_1 depends on $R_1 = R_S/D$, and R_S changes with temperature; therefore, adjusting D with temperature will ensure that R_1 remains constant at different temperatures. We fabricated and measured the microwave absorption performance of three VO_2 absorber samples with D values of 20%, 50%, and 100% to verify that the near unity absorption temperature can be adjusted using D. For the patterned VO_2 film shown in Fig. 1(a), to obtain different D values, we changed only the linewidth of the ring w. Figs. 5(a)–(f) and Fig. S16 in Appendix A show that all the fabricated VO_2 absorber samples achieved more than 99.99% peak absorption, thermally tunable absorption performance, and large modulation depth.

To evaluate the relationship between D and the near-unity absorption temperature, we extracted the temperature-dependent RL of the fabricated VO_2 absorber samples at a near-unity absorption frequency point, as shown in Fig. 5(g). The near-unity absorption temperature increased with decreasing D, indicating that varying D adjusts the temperature for the near-unity absorption and tuning range.

Next, we examined the RL of the D-ITO absorber sample (same as the VO_2 absorber, without the patterned VO_2 film) as shown by the purple lines in Fig. 5(g) and Fig. S17 in Appendix A for comparison, to further reveal that the thermally tunable absorption performance of the proposed absorber is attributed to the introduction of the patterned VO_2 film. A slight change in the peak RL for the D-ITO absorber sample was observed at varying temperatures due to the increased temperature that enhanced the electron activity. Additionally, the RL of quartz glass of the same thickness as the Cu foil (brown lines in Fig. 5(g) and Fig. S18 in Appendix A) changed slightly at different temperatures, indicating that quartz glass barely affects the measurements.

5. Discussion and conclusions

In practice, complex electromagnetic environments have become interested in microwave absorbers. To achieve the optical transmittance required in many application scenarios, an ideal transparent microwave absorber should have a high optical

transmittance. However, transparent microwave absorbers have limited application due to the lack of tunable absorption performance and large modulation depth. Therefore, realizing a microwave absorber with tunable microwave absorption, high optical transmittance, and a large modulation depth is challenging. The main objective of this study was to realize a transparent thermally tunable microwave absorber prototype based on a patterned VO_2 film that simultaneously exhibits a high optical transmittance, a thermally tunable microwave absorption performance, a large modulation depth, and an adjustable temperature tuning range. Numerical calculations and experimental results demonstrate that the proposed VO_2 absorber achieved an 84.900% normalized optical transmittance at 620.000 nm, a near unity (99.993%) absorption peak at 15.060 GHz, and a large modulation depth (55.922 dB) by controlling the temperature from 303.150 to 523.750 K. Furthermore, the temperature for near-unity absorption and its tuning range can be adjusted by varying the VO_2 film duty cycle.

The impedance matching and temperature-dependent sheet resistance of the VO_2 films cause thermally tunable microwave absorption. Unlike other VO_2 absorbers that are opaque and mainly operate in the terahertz or infrared bands, the VO_2 film in this study was used for the first time in a transparent microwave absorber, and the mechanism of thermally tunable absorption performance was thoroughly analyzed. Additionally, although the patterned VO_2 films play a vital role and form the basis of the proposed absorber prototype, a range of different materials can be used for the transparent substrate and transparent reflective layer to meet the requirements of particular applications. According to the design principle, near-unity absorption can also be extended to other frequencies by controlling the transparent substrate optical thickness, further extending the applicability of this absorber.

In summary, the proposed transparent thermally tunable microwave absorber prototype offers new opportunities for realizing promising transparent, tunable, near-unity microwave absorbers with many potential applications, such as those in temperature sensors, thermal emitters, thermal imaging, and photovoltaic devices.

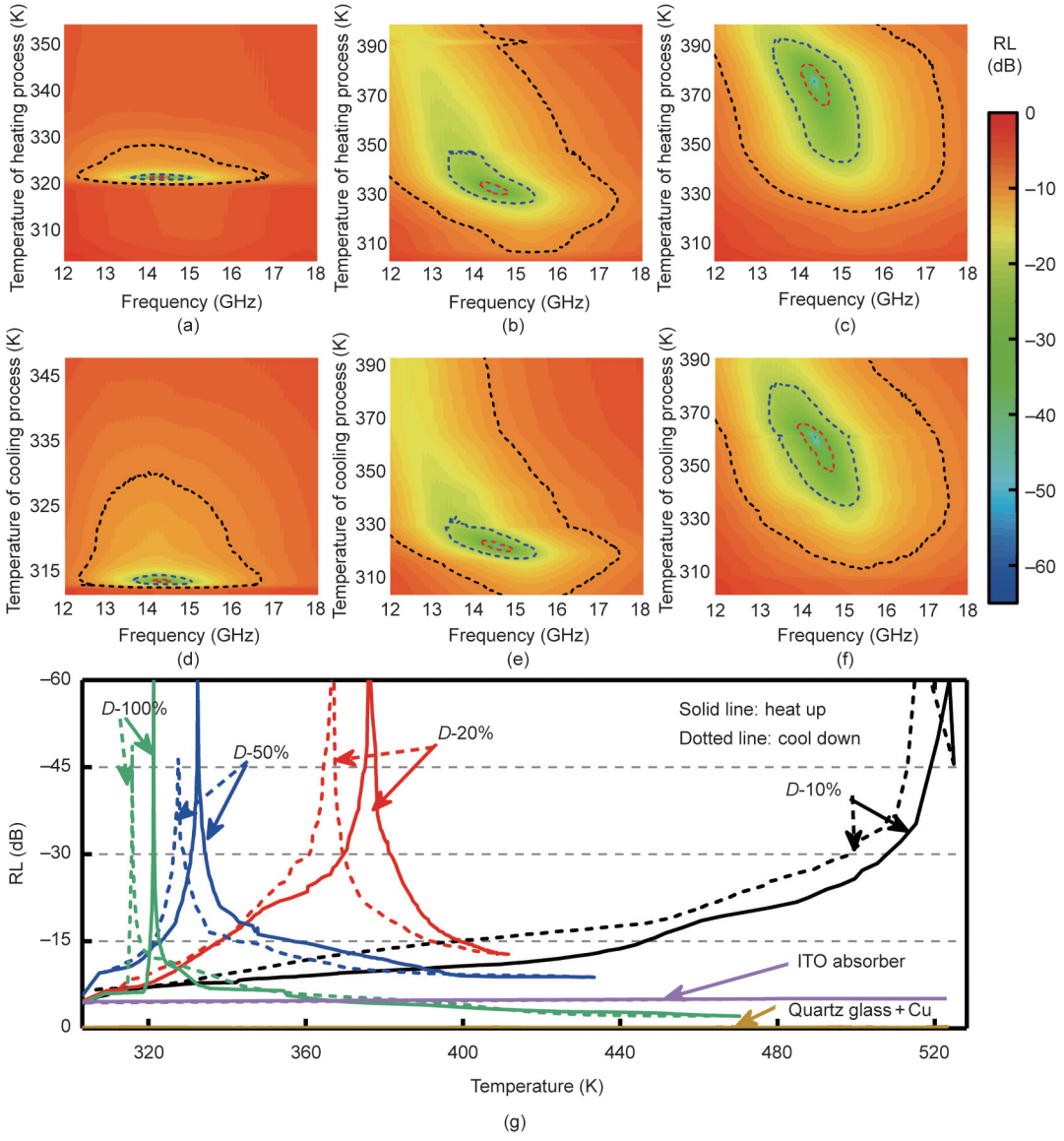

Fig. 5. Temperature and *D*-value dependence of the RL of the fabricated samples. Contour plots of the RL versus frequency and temperature of the fabricated VO_2 absorber sample during the heating process with *D* values of (a) 100%, (b) 50%, and (c) 20%. Contour plots of the RL versus frequency and temperature of the fabricated VO_2 absorber sample during the cooling process with *D* values of (d) 100%, (e) 50%, and (f) 20%. The contour lines of −10, −20, and −30 dB are plotted with black, blue, and red dashed lines, respectively. (g) Temperature-dependent RL of the fabricated VO_2 absorber samples at a near-unity absorption frequency point. *D*: duty cycle of the VO_2 film.

Acknowledgments

We acknowledge support from the National Natural Science Foundation of China (61975046).

Compliance with ethics guidelines

Zhengang Lu, Yilei Zhang, Heyan Wang, Chao Xia, Yunfei Liu, Shuliang Dou, Yao Li, and Jiubin Tan declare that they have no conflict of interest or financial conflicts to disclose.

Appendix A. Supplementary data

Supplementary data to this article can be found online at https://doi.org/10.1016/j.eng.2022.10.005.

References

[1] Zeissler K. Self-sufficient sensors operating in blood. Nat Electron 2021;4(9):629.
[2] Wen F, Zhang Z, He T, Lee C. AI enabled sign language recognition and VR space bidirectional communication using triboelectric smart glove. Nat Commun 2021;12:5378.
[3] Mei P, Lin XQ, Yu JW, Boukarkar A, Zhang PC, Yang ZQ. Development of a low radar cross section antenna with band-notched absorber. IEEE Trans Antennas Propag 2018;66(2):582–9.
[4] Chen Z, Xu C, Ma C, Ren W, Cheng HM. Lightweight and flexible graphene foam composites for high-performance electromagnetic interference shielding. Adv Mater 2013;25(9):1296–300.
[5] Cheng Y, Seow JZY, Zhao H, Xu ZJ, Ji G. A flexible and lightweight biomass-reinforced microwave absorber. Nano Micro Lett 2020;12(1):125.
[6] Miranda FA, Subramanyam G, van Keuls FW, Romanofsky RR, Warner JD, Mueller CH. Design and development of ferroelectric tunable microwave components for Ku- and K-band satellite communication systems. IEEE Trans Microw Theory Tech 2000;48(7):1181–9.
[7] Emerson W. Electromagnetic wave absorbers and anechoic chambers through the years. IEEE Trans Antennas Propag 1973;21(4):484–90.
[8] Iwaszczuk K, Strikwerda AC, Fan K, Zhang X, Averitt RD, Jepsen PU. Flexible metamaterial absorbers for stealth applications at terahertz frequencies. Opt Express 2012;20(1):635–43.
[9] Liang L, Gu W, Wu Y, Zhang B, Wang G, Yang Y, et al. Heterointerface engineering in electromagnetic absorbers: new insights and opportunities. Adv Mater 2022;34(4):2106195.
[10] Zhao Y, Hao L, Zhang X, Tan S, Li H, Zheng J, et al. A novel strategy in electromagnetic wave absorbing and shielding materials design: multi-responsive field effect. Small Sci 2022;2(2):2100077.
[11] Lv H, Yang Z, Ong SJH, Wei C, Liao H, Xi S, et al. A flexible microwave shield with tunable frequency-transmission and electromagnetic compatibility. Adv Funct Mater 2019;29(14):1900163.
[12] Lu MM, Cao MS, Chen YH, Cao WQ, Liu J, Shi HL, et al. Multiscale assembly of grape-like ferroferric oxide and carbon nanotubes: a smart absorber prototype varying temperature to tune intensities. ACS Appl Mater Interfaces 2015;7(34):19408–15.
[13] Wen B, Cao M, Lu M, Cao W, Shi H, Liu J, et al. Reduced graphene oxides: light-weight and high-efficiency electromagnetic interference shielding at elevated temperatures. Adv Mater 2014;26(21):3484–9.
[14] Shen B, Zhai W, Zheng W. Ultrathin flexible graphene film: an excellent thermal conducting material with efficient EMI shielding. Adv Funct Mater 2014;24(28):4542–8.
[15] Kim DG, Choi JH, Choi DK, Kim SW. Highly bendable and durable transparent electromagnetic interference shielding film prepared by wet sintering of silver nanowires. ACS Appl Mater Interfaces 2018;10(35):29730–40.
[16] Hu D, Cao J, Li W, Zhang C, Wu T, Li Q, et al. Optically transparent broadband microwave absorption metamaterial by standing-up closed-ring resonators. Adv Opt Mater 2017;5(13):1700109.
[17] Zhang C, Yang J, Cao W, Yuan W, Ke J, Yang L, et al. Transparently curved metamaterial with broadband millimeter wave absorption. Photon Res 2019;7(4):478–85.
[18] Wang G, Zhao Y, Yang F, Zhang Y, Zhou M, Ji G. Multifunctional integrated transparent film for efficient electromagnetic protection. Nano Micro Lett 2022;14:65.
[19] Wang H, Zhang Y, Ji C, Zhang C, Liu D, Zhang Z, et al. Transparent perfect microwave absorber employing asymmetric resonance cavity. Adv Sci 2019;6(19):1901320.
[20] Lai S, Wu Y, Wang J, Wu W, Gu W. Optical-transparent flexible broadband absorbers based on the ITO–PET–ITO structure. Opt Mater Express 2018;8(6):1585–92.
[21] Li L, Xi R, Liu H, Lv Z. Broadband polarization-independent and low-profile optically transparent metamaterial absorber. Appl Phys Express 2018;11(5):052001.
[22] Min P, Song Z, Yang L, Dai B, Zhu J. Transparent ultrawideband absorber based on simple patterned resistive metasurface with three resonant modes. Opt Express 2020;28(13):19518–30.
[23] Huang C, Zhao B, Song J, Guan C, Luo X. Active transmission/absorption frequency selective surface with dynamical modulation of amplitude. IEEE Trans Antennas Propag 2021;69(6):3593–8.
[24] Huang C, Song J, Ji C, Yang J, Luo X. Simultaneous control of absorbing frequency and amplitude using graphene capacitor and active frequency-selective surface. IEEE Trans Antennas Propag 2021;69(3):1793–8.
[25] Qian C, Zheng B, Shen Y, Jing L, Li E, Shen L, et al. Deep-learning-enabled self-adaptive microwave cloak without human intervention. Nat Photonics 2020;14(6):383–90.
[26] Li Y, Lin J, Guo H, Sun W, Xiao S, Zhou L. A tunable metasurface with switchable functionalities: from perfect transparency to perfect absorption. Adv Opt Mater 2020;8(6):1901548.
[27] Luo Z, Long J, Chen X, Sievenpiper D. Electrically tunable metasurface absorber based on dissipating behavior of embedded varactors. Appl Phys Lett 2016;109(7):071107.
[28] Wu T, Li W, Chen S, Guan J. Wideband frequency tunable metamaterial absorber by splicing multiple tuning ranges. Results Phys 2021;20:103753.
[29] Zhang J, Wei X, Rukhlenko ID, Chen HT, Zhu W. Electrically tunable metasurface with independent frequency and amplitude modulations. ACS Photonics 2019;7(1):265–71.
[30] Balci O, Polat EO, Kakenov N, Kocabas C. Graphene-enabled electrically switchable radar-absorbing surfaces. Nat Commun 2015;6:6628.
[31] Zhang J, Liu Z, Lu W, Chen H, Wu B, Liu Q. A low profile tunable microwave absorber based on graphene sandwich structure and high impedance surface. Int J RF Microw Comput Aided Eng 2020;30(2):e22022.
[32] Lu WB, Wang JW, Zhang J, Liu ZG, Chen H, Song WJ, et al. Flexible and optically transparent microwave absorber with wide bandwidth based on graphene. Carbon 2019;152:70–6.
[33] Wu S, Zha D, Miao L, He Y, Jiang J. Graphene-based single-layer elliptical pattern metamaterial absorber for adjustable broadband absorption in terahertz range. Phys Scr 2019;94(10):105507.
[34] Zhang J, Li Z, Shao L, Zhu W. Dynamical absorption manipulation in a graphene-based optically transparent and flexible metasurface. Carbon 2021;176:374–82.
[35] Grande M, Bianco GV, Perna FM, Capriati V, Capezzuto P, Scalora M, et al. Reconfigurable and optically transparent microwave absorbers based on deep eutectic solvent-gated graphene. Sci Rep 2019;9:5463.
[36] Wu B, Tuncer HM, Naeem M, Yang B, Cole MT, Milne WI, et al. Experimental demonstration of a transparent graphene millimetre wave absorber with 28% fractional bandwidth at 140 GHz. Sci Rep 2015;4:4130.
[37] Zhang H, Hu C, Yang J, Tang L, Huang D, Shao L, et al. Graphene-based active frequency selective surface in microwave frequency. J Appl Phys 2019;125(9):094501.
[38] Huang Y, Wen G, Zhu W, Li J, Si LM, Premaratne M. Experimental demonstration of a magnetically tunable ferrite based metamaterial absorber. Opt Express 2014;22(13):16408–17.
[39] Lei M, Feng N, Wang Q, Hao Y, Huang S, Bi K. Magnetically tunable metamaterial perfect absorber. J Appl Phys 2016;119(24):244504.
[40] Lv JF, Ding C, Meng FY, Han JQ, Jin T, Wu Q. A tunable metamaterial absorber based on liquid crystal with the compact unit cell and the wideband absorption. Liq Cryst 2021;48(10):1438–47.
[41] Gao S, Yang J, Wang P, Zheng A, Lu H, Deng G, et al. Tunable liquid crystal based phase shifter with a slot unit cell for reconfigurable reflectarrays in F-band. Appl Sci 2018;8(12):2528.
[42] Ren Z, Cheng L, Hu L, Liu C, Jiang C, Yang S, et al. Photoinduced broad-band tunable terahertz absorber based on a VO_2 thin film. ACS Appl Mater Interfaces 2020;12(43):48811–9.
[43] Ding F, Zhong S, Bozhevolnyi SI. Vanadium dioxide integrated metasurfaces with switchable functionalities at terahertz frequencies. Adv Opt Mater 2018;6(9):1701204.
[44] Jeong YG, Bahk YM, Kim DS. Dynamic terahertz plasmonics enabled by phase-change materials. Adv Opt Mater 2019;8(3):19005488.
[45] Zhong M. Modulation of a multi-band tunable metamaterial with metal disk array. Opt Mater 2020;106:110023.
[46] Liu Y, Qian Y, Hu F, Jiang M, Zhang L. A dynamically adjustable broadband terahertz absorber based on a vanadium dioxide hybrid metamaterial. Results Phys 2020;19:103384.
[47] Li X, Tang S, Ding F, Zhong S, Yang Y, Jiang T, et al. Switchable multifunctional terahertz metasurfaces employing vanadium dioxide. Sci Rep 2019;9:5454.
[48] Mao M, Liang Y, Liang R, Zhao L, Xu N, Guo J, et al. Dynamically temperature–voltage controlled multifunctional device based on VO_2 and graphene hybrid metamaterials: perfect absorber and highly efficient polarization converter. Nanomaterials 2019;9(8):1101.
[49] Chandra S, Franklin D, Cozart J, Safaei A, Chanda D. Adaptive multispectral infrared camouflage. ACS Photonics 2018;5(11):4513–9.
[50] Kort-Kamp WJM, Kramadhati S, Azad AK, Reiten MT, Dalvit DAR. Passive radiative "thermostat" enabled by phase-change photonic nanostructures. ACS Photonics 2018;5(11):4554–60.
[51] Lyu X, Heßler A, Wang X, Cao Y, Song L, Ludwig A, et al. Combining switchable phase-change materials and phase-transition materials for thermally regulated smart mid-infrared modulators. Adv Opt Mater 2021;9(16):2100417.

[52] Wang Q, Shen B, Huang J, Yang H, Pei G, Yang H. A spectral self-regulating parabolic trough solar receiver integrated with vanadium dioxide-based thermochromic coating. Appl Energy 2021;285:116453.
[53] Rensberg J, Zhang S, Zhou Y, McLeod AS, Schwarz C, Goldflam M, et al. Active optical metasurfaces based on defect-engineered phase-transition materials. Nano Lett 2016;16(2):1050–5.
[54] Zhu Z, Evans PG, Haglund Jr RF, Valentine JG. Dynamically reconfigurable metadevice employing nanostructured phase-change materials. Nano Lett 2017;17(8):4881–5.
[55] Kang T, Ma Z, Qin J, Peng Z, Yang W, Huang T, et al. Large-scale power-efficient Au/VO_2 active metasurfaces for ultrafast optical modulation. Nanophotonics 2020;10(2):909–18.
[56] Wang JN, Xiong B, Peng RW, Li CY, Hou BQ, Chen CW, et al. Flexible phase change materials for electrically-tuned active absorbers. Small 2021;17(31):2101282.
[57] Negm A, Bakr M, Howlader M, Ali S. Switching plasmonic resonance in multi-gap infrared metasurface absorber using vanadium dioxide patches. Smart Mater Struct 2021;30(7):075011.
[58] Zhang Y, Dong H, Mou N, Chen L, Li R, Zhang L. High-performance broadband electromagnetic interference shielding optical window based on a metamaterial absorber. Opt Express 2020;28(18):26836–49.
[59] Rahmanzadeh M, Rajabalipanah H, Abdolali A. Analytical investigation of ultrabroadband plasma–graphene radar absorbing structures. IEEE Trans Plasma Sci 2017;45(6):945–54.